RESEARCH ARTICLE

Key Points:
- Wet olivine rheology with varied water content is employed to investigate the weakening effect of cratonic lithosphere
- Hydration weakening of the cratonic lithosphere promotes convective instability and lithospheric mantle dripping
- Convective lithospheric mantle dripping results in significant lithospheric thinning beneath cratons

Correspondence to:
J. Liao,
jie.liao@erdw.ethz.ch

Modeling Craton Destruction by Hydration-Induced Weakening of the Upper Mantle

Jie Liao[1] (ID)**, Qin Wang**[2] (ID)**, Taras Gerya**[1]**, and Maxim D. Ballmer**[1] (ID)

[1]Geophysical Fluid Dynamics, Institute of Geophysics, ETH Zurich, Zurich, Switzerland, [2]State Key Laboratory for Mineral Deposits Research, Department of Earth Sciences, Nanjing University, Nanjing, China

Abstract Growing evidence shows that lithospheric mantle beneath cratons may contain a certain amount of water that originated from dehydration of subducted slabs or mantle metasomatism. As water can significantly reduce the viscosity of nominally anhydrous minerals such as olivine, hydration-induced rheological weakening is a possible mechanism for the lithospheric thinning of cratons. Using 2-D thermomechanical numerical models, we investigated the influence of water on dislocation and diffusion creep of olivine during the evolution of cratonic lithosphere. Modeling results indicate that dislocation creep of wet olivine alone is insufficient to trigger dramatic lithospheric thinning within a timescale of tens of millions of years, even with an extremely high water content. However, if diffusion creep is incorporated, significant convective instability will occur at the base of the lithosphere and drive lithospheric mantle dripping, which results in intense lithospheric thinning. We performed semianalytical models to better understand the influence of various parameters on the onset of convective instability. The convective instability promoted by hydration weakening drives lithospheric mantle dripping beneath cratons and thus provides a possible mechanism for cratonic thinning.

Plain Language Summary Mechanisms and processes of craton destruction are the subjects of ongoing debates. Growing evidence indicates that the cratonic lithosphere contains a certain amount of water. Although deformation experiments demonstrated significant weakening effects of water on the viscosity of nominally anhydrous minerals such as olivine, how water distribution affects the craton evolution is not clear. In this study, we used experimentally determined flow laws of dry and wet olivine, to systematically investigate hydration-induced weakening on the dynamics of the cratonic lithosphere. Our numerical modeling results indicate that the combined contribution of dislocation and diffusion creep of wet olivine can generate lithospheric mantle dripping at the base of the lithosphere due to convective instability, which results in significant lithospheric thinning. Therefore, hydration-driven weakening is an important mechanism of craton destruction as well as intracontinental lithospheric thinning.

1. Introduction

Although most cratons remain stable since the formation of the thick lithospheric keels, some exceptions are present. For example, the North China craton (Menzies et al., 2007), the North Atlantic craton (Tappe et al., 2007), and the Wyoming craton (Carlson et al., 2004) have experienced dramatic lithospheric deformation/thinning and magmatism in the Phanerozoic. The Tanzanian craton is subject to marginal deformation due to the surrounding active continental rifting (e.g., Weeraratne et al., 2003). Rifting events were likely involved in the San Francisco craton (e.g., Danderfer et al., 2009). The possible mechanisms (e.g. convective removal, basal traction) that may destroy the continental lithosphere have been summarized previously (e.g., Lee et al., 2011). However, destructing cratonic lithosphere is more difficult, because it is thick, cold, depleted, and rheologically strong (e.g., Foley, 2008). Previous studies have investigated several destruction mechanisms, such as small-scale convection on craton edges (He, 2014; King & Ritsema, 2000; van Wijk et al., 2010), lithospheric material dripping due to the Rayleigh-Taylor instability caused by compositional heterogeneity (Gorczyk et al., 2012), lithospheric mantle stratification (Liao & Gerya, 2014; Liao et al., 2013; O'Neill et al., 2010), lithospheric delamination due to eclogitization of the mafic lower crust (Gao et al., 2004), and thermomagmatic erosion (Foley, 2008; Koptev, 2015; Wu et al., 2005; Xu, 2001; Zhang et al., 2005). Some of the proposed mechanisms are somewhat qualitative and thus hard to appraise.

Recently, hydration of the lithospheric mantle beneath cratons is revealed based on mantle xenoliths and magnetotellurics studies (Fullea et al., 2011; Li et al., 2008; Selway et al., 2014; Wang et al., 2014; Xia et al., 2013). Water is a primary constituent of fluids from subducted slabs. With increasing pressure and temperature along subduction paths, fluids are produced by metamorphic dehydration and partial melting due to the breakdown of hydrous minerals and exsolution of structural hydroxyl and molecular water from nominally anhydrous minerals (e.g., Hacker, 2008; Zheng et al., 2016). Concentrations of dissolved silica and alkalis in H_2O is increased with depths, producing fluids in the form of aqueous solutions, hydrous melts, and supercritical fluids (e.g., Manning, 2004; Ni et al., 2017). Moderate water contents (~50 ppm H_2O by weight) in olivine (and much higher water contents in orthopyroxene and clinopyroxene) were measured in the peridotite xenoliths from the Colarado Plateau (Li et al., 2008), where hydrofluid was probably introduced into the Archean cratonic mantle through the low-angle subduction of the Farallon plate during the early Cenozoic (Figure 1a) (Dixon et al., 2004; Lee, 2005; Li et al., 2008; Smith, 2010). In the North China craton, abnormally high water content (~1,000 ppm) is estimated for the lithospheric mantle source of early Cretaceous basalts, which erupted at the destruction climax of the North China craton (Xia et al., 2013). Water was likely incorporated in the lithospheric mantle of the North China craton due to slab dehydration of the Paleo-Pacific subduction (Figure 1a) (Huang & Zhao, 2006; Menzies et al., 2007; Niu, 2005; Zhang et al., 2009) or released from the mantle transition zone perturbed by the propagation of the stagnant Pacific slab (Figure 1a) (Chen et al., 2017; Wang et al., 2016). Water transportation from the subducted slab to the mantle wedge at shallow depth (<200 km) is a fast process within several million years (e.g., Arcayet al., 2005; Faccenda et al., 2012). On the other hand, water transportation from the deep mantle (either from a stagnant oceanic slab or from the mantle transition zone) to the shallow lithosphere could be slow, but this process can be enhanced by small-scale convection at the top of a stagnant oceanic slab (Richard & Bercovici, 2009) or slab perturbation in the hydrous mantle transition zone (Wang et al., 2016). In addition, kimberlites represent localized water and CO_2 reservoirs in the upper mantle and bring episodic fluids rich in CO_2, H_2O, K^+, Na^+, and $Al3^+$ to the overlying continental lithosphere (Price et al., 2000; Sleep, 2009). Despite of sparse exposure, large amounts of kimberlites could be trapped in the cratonic lithosphere and cause hydration and carbonate metasomatism of the subcontinental lithospheric mantle (Peslier et al., 2010; Selway et al., 2014; Sleep, 2005, 2009). A concentrated midlithospheric metasomatism layer has been proposed in the North China craton (Xu, 2001). Although kimberlites provide additional evidence for high water contents, their extremely high water contents may not be representative of the average water content of the lithospheric mantle, since they may become trapped in the catatonic lithosphere and cause local hydration and carbonate metasomatism. Studies of mantle xenoliths indicate that the volume percentage of phlogopite, one of the most important hydrous silicates during mantle metasomatism, is very limited in the lithospheric mantle beneath cratons (Doucet et al., 2014). Hence, kimberlites are isolated intrusions and the extremely high water content in olivine megacrysts from kimberlites are not representative of the lithospheric mantle beneath cratons (Wang, 2010).

Large viscosity contrast between the depleted cratonic mantle and the surrounding enriched asthenospheric mantle has been regarded as one of the key parameters that ensure the long-term stability of cratons (Lenardic et al., 2003; Peslier et al., 2010). Water can dramatically reduce mantle viscosity (Figures 1b and 1c); therefore, it may significantly influence the dynamic evolution of the cratonic lithosphere. In this study, we investigate the hydration-induced weakening effect on cratonic evolution using 2-D numerical models. As the lithospheric thinning of cratons often occurs under tectonic extension, e.g., the North China craton was subjected to large-scale basin formation and magmatism in the Jurassic and early Cretaceous due to back-arc extension (Menzies et al., 2007; Wu et al., 2005; Xu et al., 2009; Zhang et al., 2005), the North Atlantic craton experienced extensive continental rifting and is now crosscut by the Labrador Sea (Tappe et al., 2007), we focus here on the lithospheric dynamics under extension.

2. Method

2.1. Numerical Method

The 2-D thermomechanical coupled numerical code I2ELVIS (Gerya & Yuen, 2003) based on finite differences and marker-in-cell techniques is used to solve the mass, momentum, and energy conservation equations in a fully staggered grid for an incompressible media (equations (1)–(6)):

$$\frac{\partial v_i}{\partial x_i} = 0 \tag{1}$$
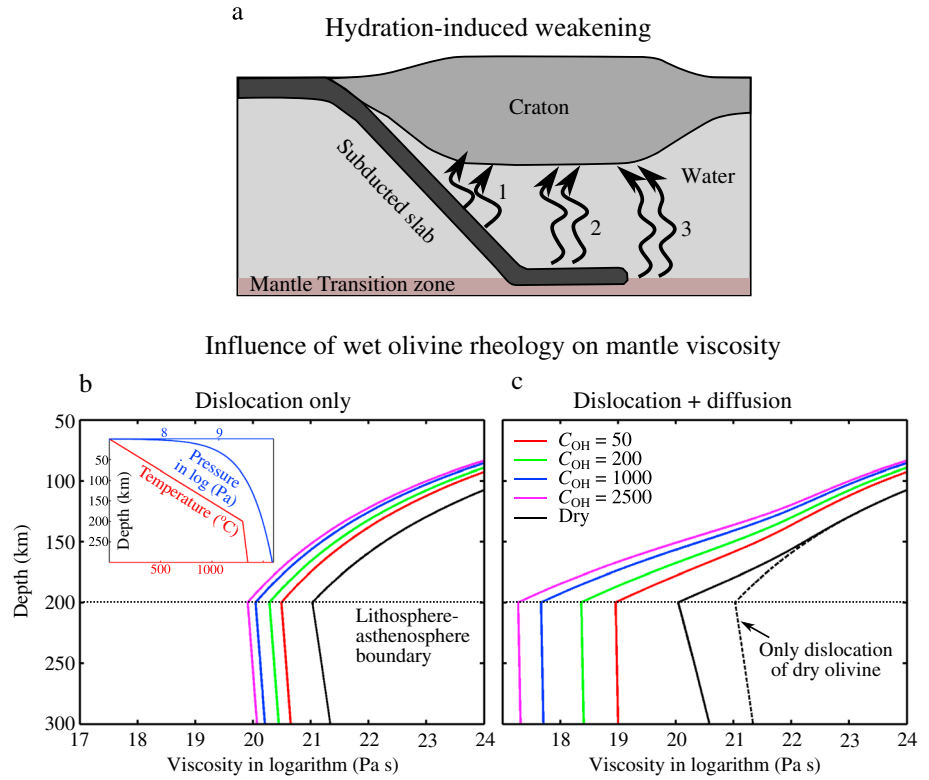
Figure 1. Hydration-induced cratonic lithosphere weakening. (a) A sketch showing the possible scenarios of cratonic lithosphere hydration through oceanic subduction (modified based on the previous studies (Faccenda, 2014; Lee et al., 2011; Wang et al., 2016). 1-Shallow slab dehydration, 2-deep slab dehydrationm and 3-water released from mantle transition zone due to slab perturbation (Wang et al., 2016). (b) Influence of water content (unit in H/10^6 Si) of wet olivine on mantle viscosity by only considering dislocation creep. (c) Influence of water content by considering both dislocation and diffusion creep. The flow law of wet olivine (Hirth & Kohlsted, 2003) is used for calculation. A constant strain rate 10^{-15} s^{-1} is assumed. Initial $P - T$ condition is shown in the inset.

$$\frac{\partial \sigma'_{ij}}{\partial x_j} - \frac{\partial P_i}{\partial x_i} = -\rho g_i \tag{2}$$

$$\rho C_p \frac{DT}{Dt} = \frac{\partial}{\partial x_i}\left(k\frac{\partial T}{\partial x_i}\right) + H \tag{3}$$

$$H = H_s + H_a + H_r + H_L \tag{4}$$

$$H_s = \sigma'_{ij}\dot{\varepsilon}_{ij} \tag{5}$$

$$H_a = T\alpha\frac{DP}{Dt} \tag{6}$$

where v is velocity, σ' the deviatoric stress tensor, P the total pressure (mean normal stress), ρ the density, g the gravitational acceleration, C_p the heat capacity, T the temperature, k the thermal conductivity, H the internal heating, H_s the shear heating, H_a the adiabatic heating, H_r the radioactive heating with a constant value for each rock, and H_L the latent heating included implicitly by increasing the effective heat capacity and thermal expansion of the partially crystallized/molten rocks (Burg & Gerya, 2005), α the thermal expansion. The Einstein notation is used for the indexes i and j, which denote spatial directions $i = (x, y)$ and $j = (x, y)$ in two dimensions.

Viscoplastic rheology is employed in our models. Plastic rheology is described by Drucker-Prager yield criterion (equation (7)), where the yielding stress (σ_y) is pressure dependent (C-rock cohesion, φ-effective friction coefficient). The viscous rheology contains both diffusion and dislocation creep (equation (8)) (Hirth & Kohlstedt, 2003; Li et al., 2008), which are temperature, pressure, and stress/strain rate-dependent (where A is preexponential constant, d is grain size, C_{OH} is water content, E_a is activation energy, V_a is activation volume,

Table 1
Rheology Parameters of Different Rocks

Type	(MPa^{-n} s^{-1})[a]	n	m	r	E_a (J/mol)	V_a (m³/mol)
Crust[b]						
Wet quartzite	3.2×10^{-4}	2.3	0	0	1.54×10^5	0
Mantle[c] (wet olivine)						
Dislocation	90	3.5	0	1.2	4.8×10^5	1.1×10^{-5}
Diffusion	1.0×10^6	1	−3	1	3.35×10^5	0.4×10^{-5}
Mantle[c] (dry olivine)						
Dislocation[e]	1.1×10^5	3.5	0	0	5.3×10^5	1.7×10^{-5}
Diffusion[e]	1.5×10^9	1	−3	0	3.75×10^5	0.6×10^{-5}

[a]Unit is MPa^{-n} s^{-1} μm^{-m} in diffusion creep. [b]Parameters are from Ranalli (1995). [c]Parameters are from Hirth and Kohlstedt (2003). [d]V_a is from Kawazoe et al. (2009). [e]V_a is from Karato et al. (1993).

R is the gas constant, and m, n, and r are experimentally determined exponents, η is viscosity, σ_{II}, $\dot{\epsilon}_{II}$, σ'_{ij}, and $\dot{\epsilon}_{ij}$ are square root of the second invariant of deviatoric stress, strain rate, deviatoric stress, and strain rate tensors, respectively). Effective viscosity of rocks (η_{eff}) is constrained by the smaller value between the plastic viscosity (η_{plas}) and viscous viscosity (η_{vis}). Viscous viscosity is also an effective value constrained by both dislocation and diffusion creep (equation (11)). Rock density is a function of composition, temperature, and pressure: $\rho = \rho_0[1 + \beta(P - P_r)][1 - \alpha(T - T_r)]$, where ρ_0 is the reference density of a given material at the reference pressure P_r (10^5 Pa) and temperature T_r (298.15 K), and β and α are the compressibility and thermal expansion, respectively. Detailed parameters are listed in Tables 1 and 2.

$$\sigma_y = C + P\varphi \tag{7}$$

$$\dot{\epsilon}_{II} = Ad^m C_{OH}^r \sigma_{II}^n \exp\left(-\frac{E_a + PV_a}{RT}\right) \tag{8}$$

$$\eta_{plas} = \frac{\sigma_y}{2\dot{\epsilon}_{II}} \tag{9}$$

$$\eta_{disl(diff)} = \frac{\sigma_{II}}{2\dot{\epsilon}_{II}} \tag{10}$$

$$\eta_{vis} = \frac{1}{1/\eta_{disl} + 1/\eta_{diff}} \tag{11}$$

$$\eta_{eff} = \min(\eta_{plas}, \eta_{vis}) \tag{12}$$

$$\sigma_{II} = \sqrt{0.5\sigma'_{ij}}, \dot{\epsilon}_{II} = \sqrt{0.5\dot{\epsilon}_{ij}}, \tag{13}$$

It is worth emphasizing that the flow law formulation (equation (8)) for olivine contains water content (C_{OH}) in units of H/10^6 Si. Water content can be converted from water fugacity (f_{H2O} in units of Pa), which is a function of temperature and pressure, and measured in water-saturated conditions (Hirth & Kohlstedt, 2003; Kohlstedt et al., 1996; Li et al., 2008; Mei & Kohlstedt, 2000a). However, mantle (maybe except the mantle wedge) is generally undersaturated in water (Hirschmann, 2006; Hirth & Kohlstedt, 2003). Thus, water fugacity is an inconvenient parameter for tracking water content in mantle in geodynamic models. A conversion from water fugacity to water content is necessary (Kohlstedt et al., 1996), and the updated flow law using water content is employed in this study (equation (8)) (Hirth & Kohlstedt, 2003; Li et al., 2008). Water content C_{OH} can be regarded as a constant value in a closed system or vary with time in an open system (Karato & Jung, 2003). In this study, we consider that the water content of olivine is constant in each model run, assuming that a certain amount of water has been instantaneously introduced to the cratonic lithosphere and is retained thereafter. For grain size-sensitive diffusion creep, we adopt a constant grain size in each model run by neglecting the change of grain size during recrystallization and annealing. Thus, the influence of water on mantle rheology is estimated by dislocation and diffusion creep of wet olivine with variable water contents. The influence of oxygen fugacity on wet olivine is ignored in this study. Based on deformation experiments, higher oxygen fugacity will increase strain rate of olivine (Tielke et al., 2017). The strain rate of wet olivine under oxygen fugacity conditions buffered by Fe/FeO (Mackwell et al., 1985) will be increased by a factor of 1.8 at 1300°C when buffered by Ni/NiO (Bai et al., 1991).

Table 2
Physical Parameters of Rock

Variable	Symbol (unit)	Crust	Mantle	References[a]
Density	$\rho_0 \left(\frac{kg}{m^3} \right)$	2,700	3,300[b]	1
Cohesion	C_o (Pa)	5×10^5	5×10^5	2
Friction coefficient	ϕ	0.4	0.6	2
Radioactive heating	$H_r \left(\frac{W}{m^3} \right)$	1.75×10^{-6}	2.2×10^{-8}	1
Latent heating	$Q_L \left(\frac{J}{kg} \right)$	3×10^5	4×10^5	1, 3
Thermal capacity	$C_p \left(\frac{J}{kg\,K} \right)$	1,000	1,000	1
Thermal expansivity	$\alpha \left(\frac{1}{K} \right)$	3×10^{-5}	3×10^{-5}	1
Compressibility	$\beta \left(\frac{1}{MPa} \right)$	1×10^{-5}	1×10^{-5}	1
Thermal conductivity[c]	$k \left(\frac{W}{mK} \right)$	$\left(1.18 + \left(\frac{474}{T+77} \right) \right) \exp(0.00004P)$	$\left(0.73 + \frac{1293}{T+77} \right) \exp(0.00004P)$	4

[a]References: 1, Turcotte and Schubert (2002); 2, Ranalli (1995); 3, Bittner and Schmeling (1995); and 4, Clauser and Huenges (1995). [b]Lithospheric mantle may have lower reference densities in different test models. Asthenospheric mantle always has the same reference density. [c]Pressure in MPa.

The molar concentration of forsterite in olivine, Mg/(Mg+Fe)×100, is defined as the Fo number of olivine. Because the flow laws of olivine came from deformation experiments on San Carlos olivine with composition of Fo_{90}, we use Fo_{90} to estimate the water content in the lithospheric mantle. The molecular weight of olivine $(Mg_{0.9} Fe_{0.1})_2SiO_4$ is 147.017 g. So water content of 1000 H/10^6 Si is equal to $1,000/2 \times 18/147.017 = 61.2$ ppm H_2O in weight. When we calculate the bulk water content in pyrolite, the hydrogen partitioning coefficient between olivine, pyroxene, and garnet should be considered (e.g., Aubaud et al., 2004), 50 ppm H_2O in olivine will correspond to 181 ppm H_2O in pyrolite (64% olivine, 15% orthopyroxene, 11% garnet, and 10% clinopyroxene). The normal upper mantle beneath mid-ocean ridges contains 50–200 ppm H_2O, whereas H_2O concentration in plume sources may range from 300 to 1,000 ppm, suggesting heterogeneous water distribution in the mantle (Hirschmann, 2006).

2.2. Model Setup

The initial model domain is composed of homogeneous compositional layers (Figures 2a and 2b). In the top of the model domain, a 20 km sticky air layer is prescribed, which ensures the free surface boundary condition (Crameri et al., 2012). The upper and lower crust has an equal thickness (20 km), underlain by the lithospheric mantle layer (160 km). Underneath the lithosphere is the asthenospheric mantle layer. In terms of the initial temperature distribution, two model setups are considered. In the first model setup (Figure 2a), horizontally homogeneous temperature distribution is prescribed. In the second model setup (Figure 2b),
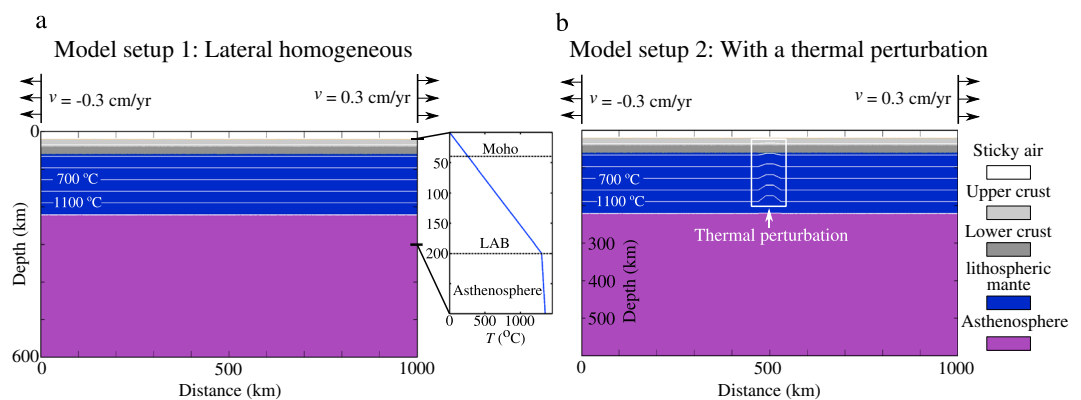
Figure 2. Initial model setup. Model setup with (a) homogeneous layers and (b) a prescribed thermal perturbation in the lithosphere. Extensional velocities are prescribed on the side boundaries. Initial temperature linearly increases in the lithosphere.
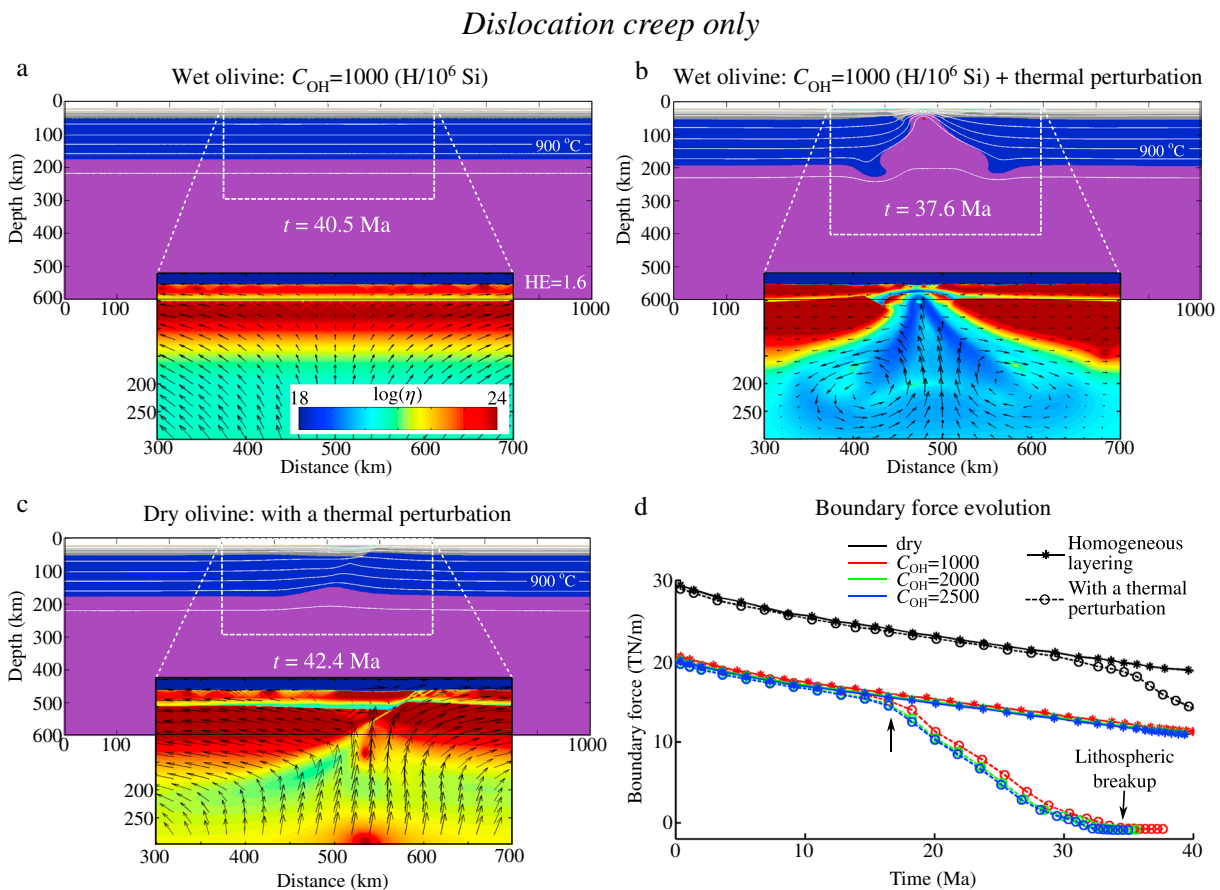
Figure 3. Model results using only dislocation creep of olivine. Composition and viscosity fields are shown. (a) Homogeneous layered model with a moderate water content of 1,000 H/10^6 Si. No strain localization after $t = 40.5$ Ma. (b) Model development with an initially imposed thermal perturbation and a moderate water content of 1,000 H/10^6 Si. Continental rifting and final breakup are developed. (c) Model results with dislocation creep of dry olivine. Continental rifting develops. (d) Evolution of boundary force influenced by water content of olivine. Black arrows in the viscosity fields illustrate the flow direction of the upper mantle. HE: horizontal exaggeration of the model domain.

a thermal perturbation is prescribed in the middle of the lithospheric domain, and this setup will produce faster strain localization.

Free slip combined with a constant (normal) velocity boundary condition is used for all the boundaries. Moderate time-independent extension rate (i.e., 0.3 cm/yr half extension rate) is uniformly prescribed on the side boundaries, and compensation velocities on the upper and lower boundaries are computed based on mass conservation (e.g., Liao & Gerya, 2014). Constant temperatures are prescribed for the upper and lower boundaries, and the thermal insulation condition (i.e., zero horizontal heat flux) is used for the side boundaries. Temperature of the 20 km thick sticky air is 0°C, initially. In the lithosphere, the initial temperature increases linearly from 0°C on the crustal surface (20 km depth) to 1,300°C at the lithosphere-asthenosphere boundary (LAB, 220 km depth). The difference between the linearly interpolated temperature profile and the one obtained through steady state temperature equation was briefly discussed in the previous study (Liao & Gerya, 2017, Figure S1), which showed that the significant difference between these two thermal profiles is only present in the upper crust, where radiogenic heating rate is larger than the underlying rock. Below the LAB, asthenospheric mantle has a small and constant gradient of 0.5°C/km initially. Material properties are listed in Table 2.
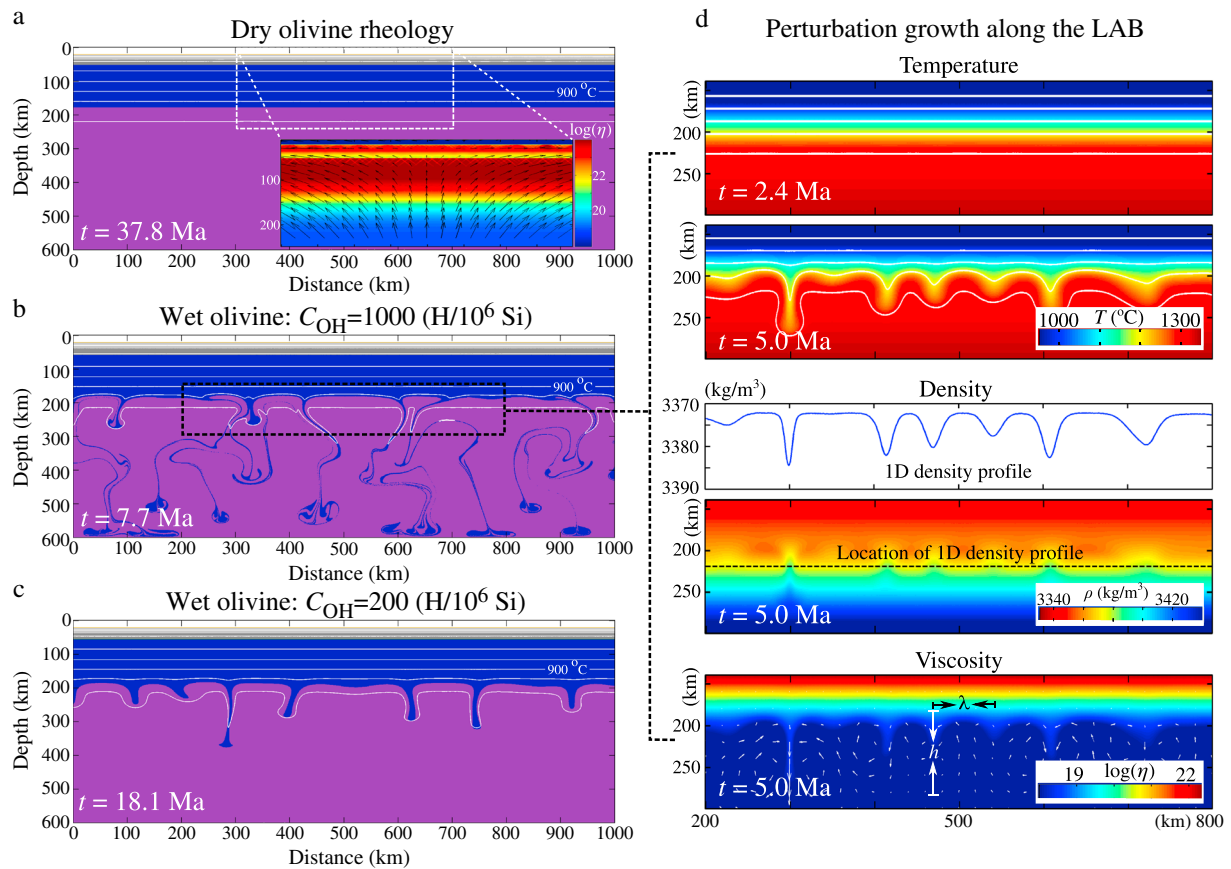
3. Modeling Results
3.1. Models With Dislocation Creep Only
In nature, both dislocation and diffusion creep are active at the same time during deformation. But they may not contribute to deformation of the crust and mantle equally, and one creep dominates deformation over

Dislocation and diffusion creep

Figure 4. Model results with both dislocation and diffusion creep for (a) dry olivine and wet olivine with a water content of (b) 1,000 H/10^6 Si and (c) 200 H/10^6 Si. (d) Perturbation growth along the LAB shown by temperature, density, and viscosity. In the viscosity snapshot, λ and h are the wavelength and thickness of the convective layer, respectively.

the other under different conditions (Burgmann & Dresen, 2008). Dislocation creep of either crustal or mantle material dominates deformation with low temperature, high stress, and large grain size (Burgmann & Dresen, 2008), which typically are lithospheric conditions. Besides, previous studies addressed that the Lehmann discontinuity (~200 km) is probably caused by a change in deformation mechanism: from dislocation creep in the shallow upper mantle producing seismic anisotropy to diffusion creep in the deep upper mantle generating isotropic structure (Karato, 1992-Karato,2010-Karato). Thus, dislocation creep may play a dominant role in the lithospheric scale. Here we first test models with only dislocation creep (Figure 3). With the homogeneous layered setup, dislocation creep does not generate significant deformation with a moderate water content of 1,000 H/10^6 Si in olivine (equal to ~60 ppm H$_2$O by weight). No strain localization occurs after 40.5 Ma (Figure 3a). The cratonic lithosphere thins homogeneously in response to the boundary extension. Increasing the water content of olivine to 2,500 H/10^6 Si has no significant effect on the deformation pattern, and the model results remain similar. For comparison, the model with a prescribed thermal perturbation generates faster strain localization and the final continental breakup occurs at 37.6 Ma (Figure 3b). However, a similar model using the dislocation creep of dry olivine and a prescribed thermal perturbation shows much slower development of continental rifting (Figure 3c).

In addition, boundary force is computed to evaluate the overall resistance of the model box to boundary extension (Brune et al., 2012, Buck et al., 1999, Liao & Gerya, 2014, Liao et al., 2013). The boundary force is calculated by integrating the normal deviatoric stress along the left and right boundaries of the lithosphere and taking the average of the two values (Figure 3d). Since the cratonic lithosphere is typically twice as thick (also cold) as normal/young continental lithosphere, the computed boundary force for the cratonic lithosphere (e.g., mean lithospheric stress of 200 MPa accounts for ~40 TN/m for a 200 km thick craton, O'Neill et al., 2008)
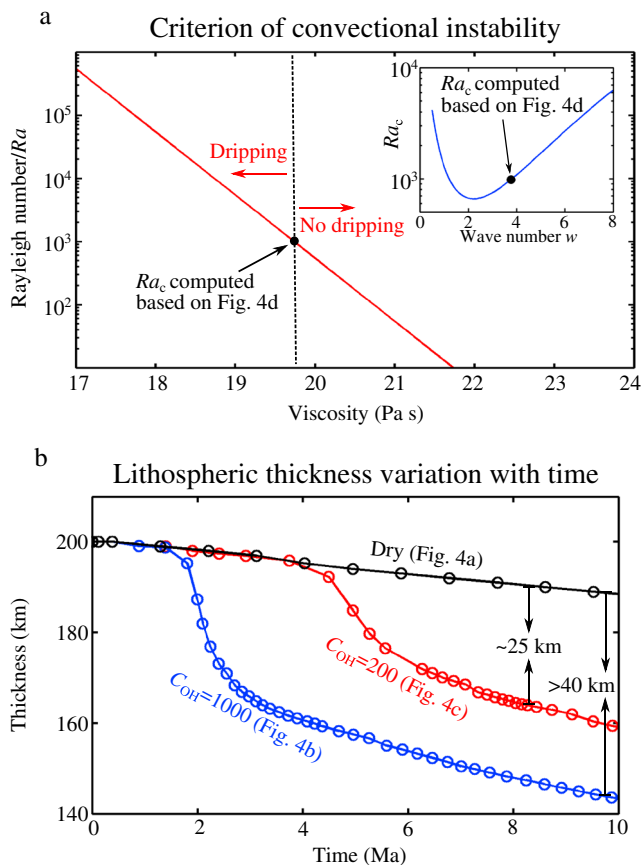
Figure 5. Lithospheric mantle dripping and thinning. (a) Lithospheric mantle dripping controlled by the Rayleigh number and the critical Rayleigh number. Both numbers are computed based on the model shown in Figure 4d. Convective instability occurs when Ra is greater than Ra_c. (b) Lithospheric thinning caused by lithospheric mantle dripping.

is typically much larger than the estimation of thin lithosphere (e.g., ~13 TN/m force for a 80 km thick lithosphere, Brune et al., 2012) and tectonic driving force (e.g., Buck, 2006). This indicates that rifting a craton is difficult in nature. Here we focus on the relative values of the boundary force affected by dry and wet olivine rheology. Two major features of the boundary force are observed from our modeling results. First, the models using the flow law of wet olivine require a smaller boundary force than the models employing the flow law of dry olivine. Second, a higher water content in olivine reduces the boundary force and produces faster strain localization if the thermal perturbation is initially imposed (the dashed color lines with open circles in Figure 3d).

Because only a small amount of H_2O can remarkably decrease the stress of dislocation creep and increase contribution of dislocation creep to the deformation of olivine (e.g., Wang, 2010), the presence of H_2O can significantly decrease the rifting force. Our model results suggest the usage of wet olivine rheology results in much weaker lithospheric mantle, and even a small amount of H_2O can remarkably decrease the stress of dislocation creep. The boundary force for rifting the cratonic lithosphere decreases by one third compared to the model using dry olivine rheology (Figure 3d). Increase of the water content does not vary boundary force significantly. This is consistent with the theoretical plot (Figure 1b), which shows the largest difference between the dry olivine line and the wet olivine lines. The difference between different wet olivine lines (e.g., COH = 1,000 and COH = 2,500) is small, particularly at low pressures (Figure 1b). Much larger influence of water content on boundary force can be expected for models employing both diffusion and dislocation creep (Figure 1c).

3.2. Models With Both Dislocation and Diffusion Creep

Contribution from the diffusion creep of olivine (assuming a constant grain size of 1 mm) is added into the homogeneous layered models (Figure 4). For dry olivine, the cratonic lithosphere thins homogeneously in response to the extension, and no strain localization occurs after ~ 38 Ma (Figure 4a). With a moderate water content of 1,000 H/10^6 Si in olivine, the model employing wet olivine rheology with both dislocation and diffusion creep produces lithospheric instabilities (Figure 4b). The lowermost lithospheric mantle drips off from the base of the lithosphere only after 7 Ma. The water content of olivine plays a key role in the initiation of lithospheric mantle dripping. A test model with 200 H/10^6 Si (~12 ppm) water content in olivine produces dripping much later and less vigorously (Figure 4c).

Convective instability (i.e., Rayleigh-Benard instability) grows along the LAB and forms small-scale convection cells, promoting lithospheric mantle dripping (Figure 4d). The initial perturbations of the convective instability grow from numerical noises (e.g., randomly distributed markers introducing small horizontal variation in density). Without the numerical noises there would be ideally no instability growth. The numerical noise could be analogous to heterogeneity within the interior of the Earth. The convective instability occurs when the Rayleigh number (Ra) is larger than the critical Rayleigh number (Ra_c) (Turcotte & Schubert, 2002), which is a function of the nondimensional wave number w ($w = 2\pi h/\lambda$, where h is the thickness of a convection layer and λ is the wavelength of a convection cell, Figures 4d and 5a). Furthermore, lithospheric thinning caused by material dripping is computed (Figure 5b). Compared to the uniform thinning in the model with dry olivine rheology, the model with wet olivine rheology generates rapid and large lithospheric thinning, and a higher water content in olivine produces stronger thinning.

3.3. Parameter Test

Model evolution is sensitive to the used parameters. Here we investigate several key parameters (the reference density of the lithospheric mantle, the temperature along the LAB, the grain size of olivine aggregates, initial lithospheric thickness, and the activation volume of mantle) and document their effects on model development (Figures 6–11).
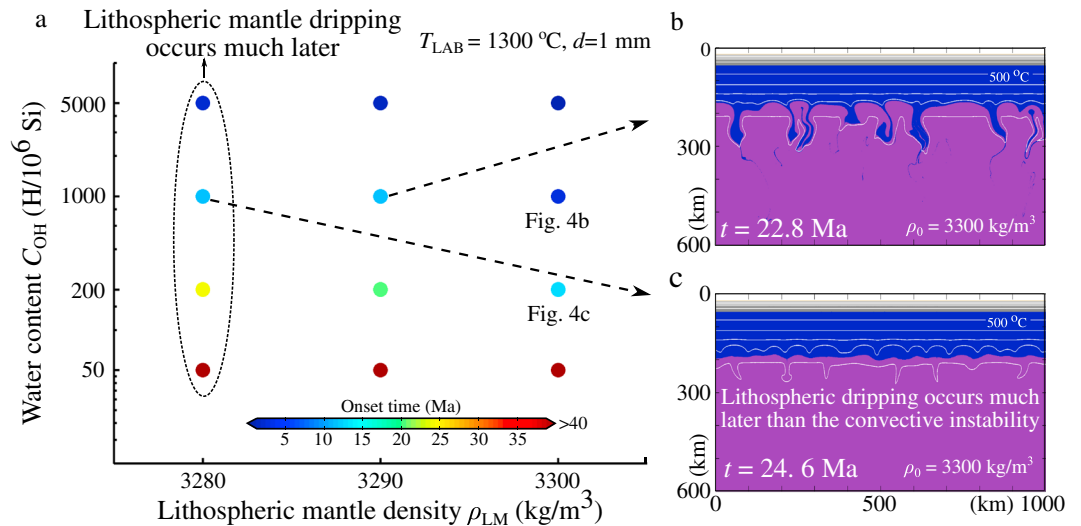
Figure 6. Influence of the reference density of the lithospheric mantle (ρ_{LM}) on model evolution with varied water contents. (a) Numerical models and (b, c) snapshots of model results. The reference density of the asthenospheric mantle (ρ_0) is 3,300 kg/m^3 in this study. The onset time of convective instability of the numerical models is determined by the rapid increase of the averaged downwelling velocities. Note that although convective instability occurs with smaller ρ_{LM}, lithospheric mantle dripping may happen much later.
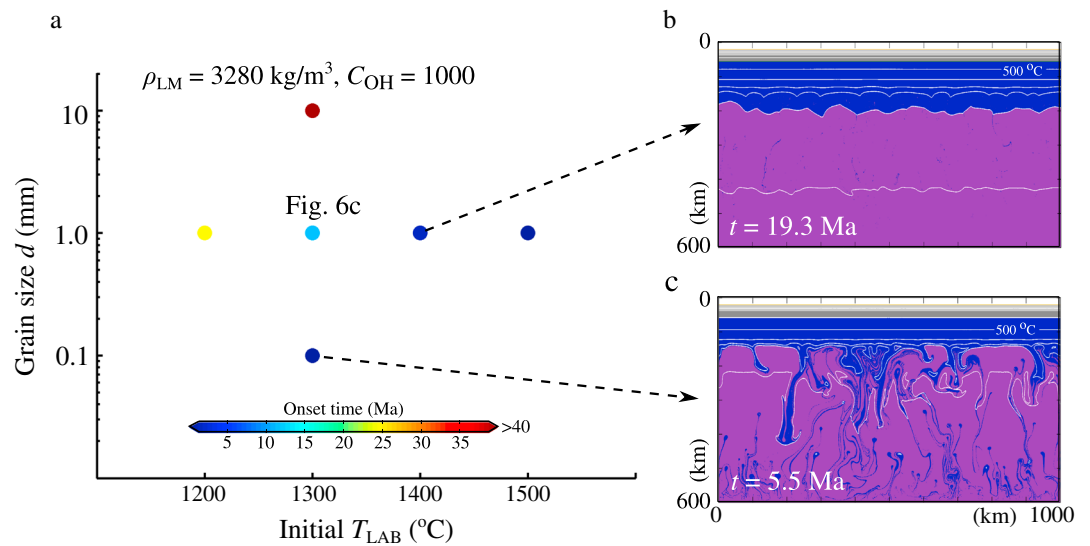
3.3.1. Reference Density of the Lithospheric Mantle

The depleted Archean cratonic mantle is commonly regarded as buoyant with several tens of kg/m^3 less denser than the underlying asthenospheric mantle (Carlson et al., 2005; Djomani et al., 2001). We test a set of models with smaller initial lithospheric mantle densities ρ_{LM} based on different water contents. It is worth emphasizing that the ρ_{LM} is the reference density at $T = 25.15°C$ and $P = 10^5$ Pa. The effective density of rocks depends on composition, temperature, and pressure, and only the temperature-dependent component of density influence the growth of the convective instability.

Model results are plotted in Figure 6. Lower reference densities of the lithospheric mantle favor later onset of convective instability (Figure 6a). With the reference density of the lithospheric mantle $\rho_{LM} = 2,90$ kg/m^3 (10 kg/m^3 smaller than the reference density of the asthenospheric mantle, which is 3,300 kg/m^3 in this study), convective instability and lithospheric mantle dripping occurs after ~11 Ma when water content in olivine reaches 1,000 H/10^6 Si (Figure 6b). In case of $\rho_{LM} = 3,280$ kg/m^3, although convective instability occurs along the base of the lithosphere at ~11 Ma, lithospheric mantle dripping occurs much later (Figure 6c). With a sufficiently small reference density of the lithospheric mantle (e.g., $\rho_{LM} = 3,250$ kg/m^3), small-scale convection occurs only in the convective layer at the base of the lithosphere without forming lithospheric mantle dripping. This is because the effective density of the lithospheric mantle (considered the thermal effect, i.e., temperature dependent) is still smaller than that of the asthenospheric mantle.

3.3.2. Initial Temperature Along the LAB

Although the cratonic lithosphere is relatively cold (Carlson et al., 2005; Menzies et al., 2007), the temperature of a cratonic root (especially at the base of the cratonic lithosphere) may change significantly due to episodic heating events during its long-term evolution. For instance, plume upwelling was proposed as an effective way of heating/weakening the base of the cratonic lithosphere (Foley, 2008; Koptev et al., 2015). Therefore, we examine the influence of initial temperatures at the LAB (T_{LAB}) on the evolution of the cratonic lithosphere. Based on the reference model (Figure 4), colder and warmer initial T_{LAB}s are tested. Cold cratonic lithosphere inhibits lithospheric dripping, while warm lithosphere promotes dripping (Figure 7). Significant dripping occurs when the cratonic lithosphere has been heated intensely (e.g., $T_{LAB} = 1,500°C$), which may happen, for example, due to plume upwelling (Foley, 2008; Koptev et al., 2015). Further discussion on the influence of the T_{LAB} on lithospheric dripping is given in section 4.1.
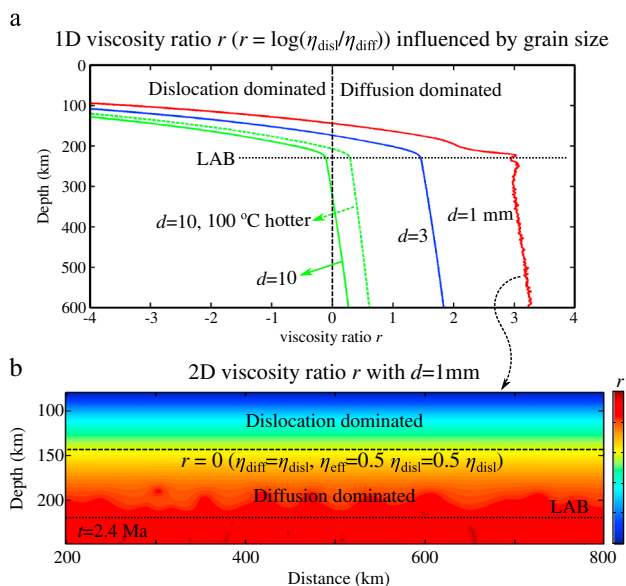
Figure 7. Influence of grain size and mantle potential temperature on lithospheric mantle dripping. (a) Numerical models and (b, c) snapshots of model results. The reference density of the lithospheric mantle and water content are labeled on the figure. The onset time of convective instability of the numerical models is determined by the rapid increase of the averaged downwelling velocities.

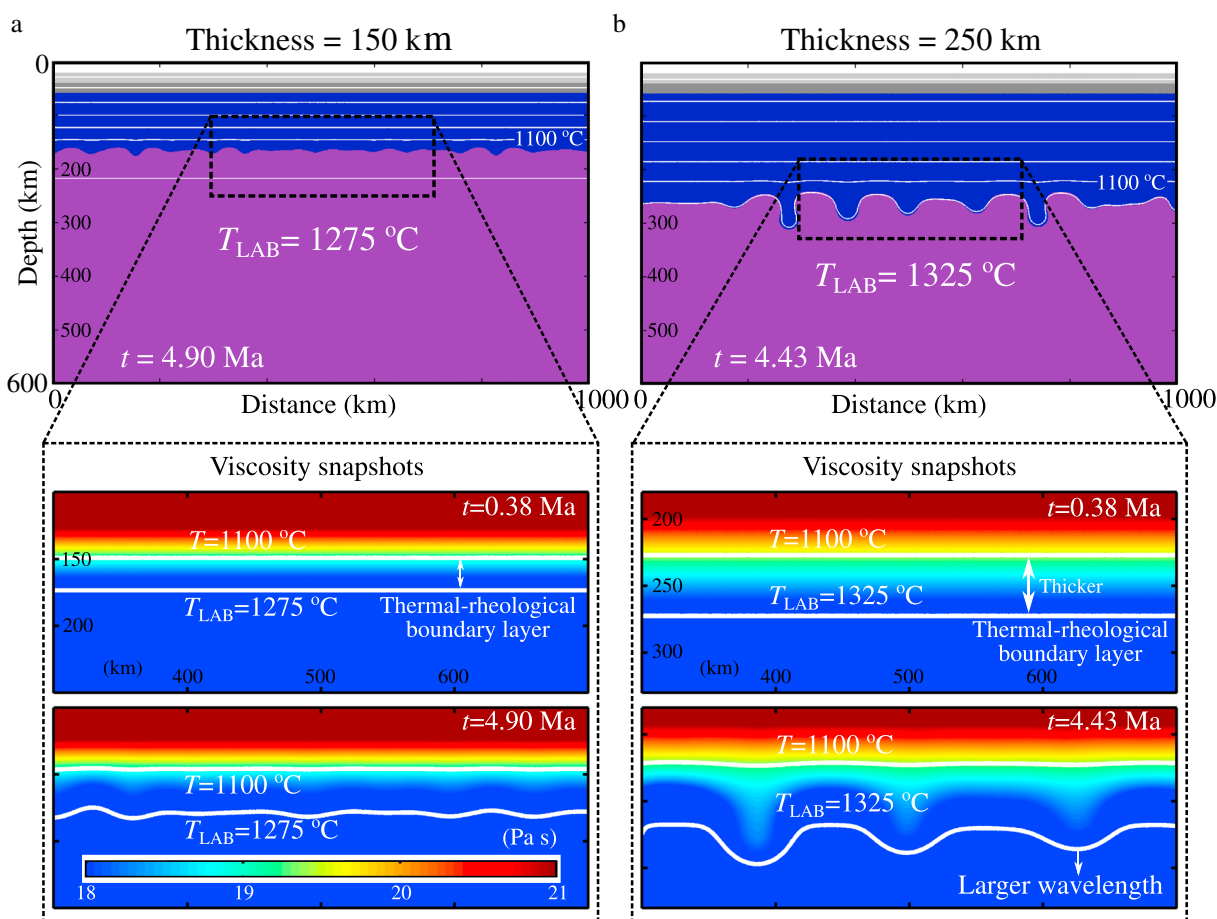### 3.3.3. Grain Size of Olivine Aggregates

Diffusion creep is grain size dependent, and a decrease in grain size of olivine aggregates results in an increase in strain rate of diffusion creep. Our model results suggest that small grain size promotes lithospheric dripping (Figure 7). The contribution from dislocation and diffusion creep is distinguished by plotting the logarithmic viscosity ratio r ($\log_{10}(\eta_{disl}/\eta_{diff})$, Figure 8). The expression $r = 0$ means η_{disl} is equal to η_{diff}, suggesting the equal contribution from dislocation and diffusion creep on mantle deformation. The $r < 0$ tells us that η_{disl} is smaller than η_{diff}, which indicates that dislocation creep is relatively fast and dominates mantle deformation. Whereas when $r > 0$, diffusion creep becomes more important than dislocation creep. Figure 8 shows a clear transition from dislocation creep-dominated deformation to diffusion creep-dominated deformation in the mantle lithosphere, and the transition depth occurs deeper for larger grain sizes. This is consistent with the deformation mechanism transition inferred from deformation maps of wet olivine (Wang, 2010). Thus, adding diffusion creep may largely enhance mantle deformation at the bottom of the lithosphere. If the grain size is sufficiently large (e.g., $d = 10$ mm), the diffusion creep will be less effective and the transition depth becomes deeper than the LAB. This indicates that in the coarse-grained lithosphere, the diffusion creep becomes less important and the lithospheric mantle dripping becomes difficult.

Figure 8. Viscosity ratio between dislocation and diffusion creep. (a) The 1-D viscosity ratio influenced by grain size. (2) The 2-D viscosity ratio with grain size $d = 1$ mm. The 1-D viscosity ratio is picked at horizontal distance $X = 500$ km and time $t = \sim 2.4$ Ma. The 2-D plot is from the model shown in Figure 4b.

Constant grain size is used in this study, which is a big assumption. Grain size is a key parameter of diffusion creep, and it largely controls the transition from dislocation-dominated to diffusion-dominated deformation. Influence of grain size evolution on lithosphere and mantle dynamics was addressed in previous studies (e.g., Gueydan & Precigout, 2014; Rozel et al., 2011). Grain size evolution is not only stress and temperature dependent (e.g., Rozel et al., 2011) but also water content dependent (Karato, 1989). A higher water content in olivine will promote rapid grain growth and reduce strain rate of diffusion creep by increasing the diffusion distance of vacancies along grain boundary (i.e., Coble creep, Karato, 1989). However, the dominant means by which hydrogen affects strain rate is to increase concentration of silicon vacancies and then facilitate dislocation climb rate (Mei & Kohlstedt, 2000b, 2000a; Tielke et al., 2017). Such water weakening

Figure 9. Influence of lithospheric thickness on model evolution. (a) An initial thinner lithosphere (150 km). (b) An initial thicker lithosphere (250 km). All other parameters (including the mantle potential temperature) are identical with the reference model shown in Figure 4b.

effect will result in strain localization and fine-grained mantle shear zones by dynamic recrystallization and, consequently, increase strain rate of diffusion creep. The trade-offs between water content and grain size evolution need to be quantitatively investigated in future studies.

3.3.4. Thickness of the Cratonic Lithosphere

The thickness of the cratonic lithosphere may affect the lithospheric dripping dynamics. It was proposed that the North China craton has experienced at least two stages of lithospheric thinning in the Late Mesozoic and Cenozoic (Xu, 2007). Multistage lithospheric thinning suggests a dramatic change in initial lithospheric structure (lithospheric thickness and thermal structure). For instance, the second stage of the lithospheric thinning may start from a relatively thin and warm lithosphere in the North China craton. Thus, it is worth testing the influence of varied initial lithospheric thickness on the model evolution.

We conducted two numerical models with a thinner (150 km) and a thicker (250 km) cratonic lithosphere (compared to the reference model), respectively (Figure 9). We keep the mantle potential temperatures in these two models (T_{LAB} = 1,275°C and T_{LAB} = 1,325°C, respectively) the same with the reference model (i.e., T_{LAB} = 1300°C). Thus, the only varied parameter is the lithospheric thickness. Both models produce lithospheric mantle dripping due to convective instability (Figure 9). The model with a thicker lithosphere generates earlier and more vigorous lithospheric dripping (Figure 9b), mainly because its thicker convective layer (e.g., Sleep, 2007). This thicker convective layer advances convective instability, because it tends to form relatively large wavelength of convection cells and larger Rayleigh numbers (see detailed discussion in section 4.1).

### 3.3.5. Activation Volume of Mantle

Activation volume (V_a) of mantle rheology may play an important role on asthenospheric mantle dynamics because of large pressure at great depth. A big range of uncertainty is given for the activation volume of
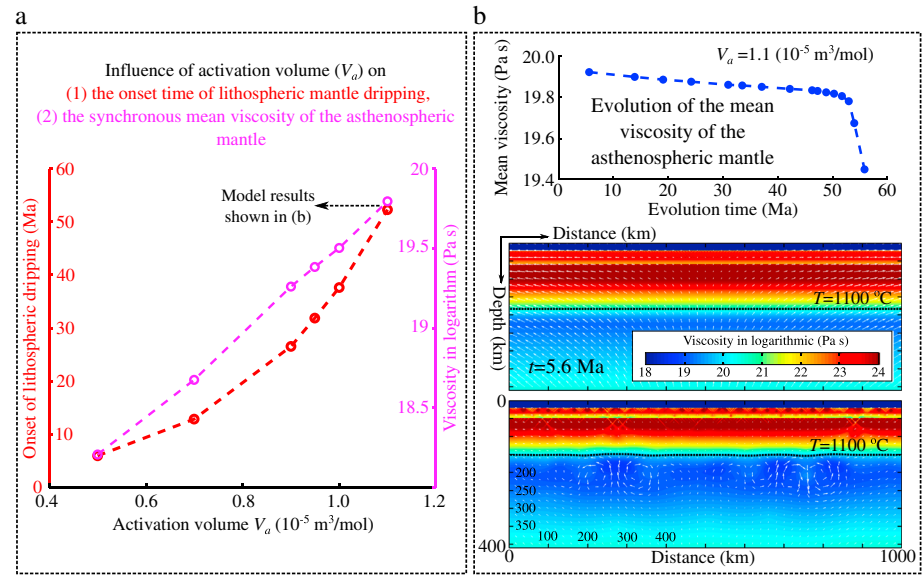
Figure 10. Influence of mantle activation volume on lithospheric mantle dripping. (a) Effect of activation volume on the onset time of lithospheric mantle dripping and the synchronous mean viscosity of the asthenospheric mantle. (b) Evolution of the mean asthenospheric mantle viscosity and the temporal model snapshots shown in viscosity. Data used for averaging asthenospheric mantle viscosity is picked by using a temperature threshold ($T > 1,100°C$), which typically defines the upper boundary of a convective layer.

mantle (Hirth & Kohlstedt, 2003). The activation volume of olivine determined by deformation experiments shows large variations from $0 \pm 0.5 \times 10^{-5}$ m^3/mol (Li et al., 2006) to 2.7×10^{-5} m^3/mol (Borch & Green, 1989) and decreases with increasing pressure (Hirth & Kohlstedt, 2003). The highest-resolution mechanical data are acquired at ~300 MPa in most deformation experiments, while the pressure of the upper mantle are 2–12 GPa. Therefore, over the entire upper mantle, the effect of pressure on viscosity can be as large as several orders of magnitude, and it is important to test the influence of the activation volume of olivine on cratonic evolution.

According to the summary of Hirth and Kohlstedt (2003), the activation volume we used for dislocation and diffusion creep of wet olivine is 1.1×10^{-5} m^3/mol and 0.4×10^{-5} m^3/mol, respectively (Table 1). In this set of experiments, we use the same activation volume for both dislocation and diffusion creep (Figure 10). An increase in activation volume results in a significant delay of lithospheric dripping and larger mean viscosity of
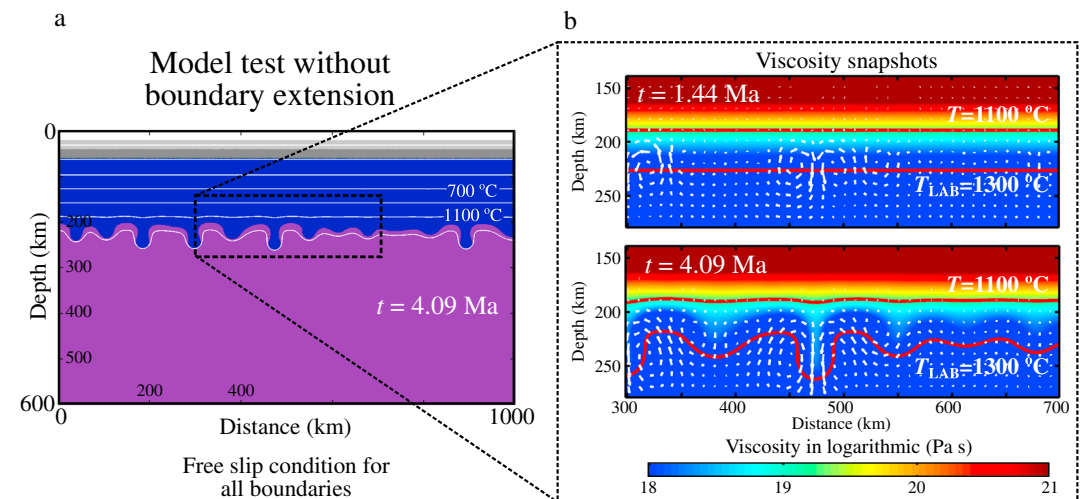
Figure 11. Model test without boundary extension. (a) Model result shown by lithology. Velocity boundary condition is free slip for all boundaries. (b) Temporal evolution of lithospheric mantle dripping shown by viscosity snapshots. Two isothermal lines are marked. White arrows are velocity vectors.

the asthenospheric mantle (Figure 10a). With a larger activation volume ($V_a = 1.1 \times 10^{-5}$ m^3/mol, Figure 10b), viscosity of the asthenospheric mantle becomes more realistic than that in the previous models (Figure 4b). The mean viscosity of the asthenospheric mantle is around 10^{20} Pa s, which is close to the mantle viscosity from the base of the lithosphere to 410 km estimated from joint inversion of mantle convection, mineral physics, and postglacial rebounding observations (Mitrovica & Forte, 2004; Steinberger & Calderwood, 2006). The mean asthenospheric mantle viscosity decreases gradually followed by a dramatic decrease due to the onset of lithospheric dripping.

3.4. Model Test Without Boundary Extension

We initiate the 2-D numerical modeling by applying boundary extension in this study, since some deformed cratons experienced intense tectonic extension, such as the typical example of the North China craton, which was subjected to large-scale basin formation and pervasive magmatism in the Jurassic and early Cretaceous due to back-arc extension (Menzies et al., 2007; Wu et al., 2005; Xu et al., 2009; Zhang et al., 2005). Here we test a model without boundary extension based on the reference model, and velocity boundary condition is free slip for all boundaries (Figure 11). Model results show that convective instability occurs in the convective layer at the base of the lithosphere, promoting lithospheric mantle dripping. This indicates that boundary extension is not a necessary condition for the initiation and development of convective instability. Moreover, this model produces earlier convective instability than the reference model (Figure 11b), because the convective layer in the reference model is continuously thinning as a response to the boundary extension (see more discussion in section 4.1). As aforementioned, the computed boundary force for rifting the cratonic lithosphere (Figure 3d) is much larger than the available tectonic force (e.g., Buck, 2006). Lithospheric thinning of cratons through rifting can be considerable difficult in nature. Convective lithospheric mantle dripping could thus be an effective way of cratonic lithospheric thinning, occurrence of which does not rely on tectonic extension.

4. Discussion

4.1. Semianalytical Models of the Onset of Convective Instability

In order to benchmark our numerical models and further understand the influence of various parameters (i.e., water content C_{OH}, the reference density of the lithospheric mantle ρ_{LM}, grain size d, and the temperature at the LAB T_{LAB}), we explore the conditions for convective instability using semianalytic models (i.e., similar to Motoki & Ballmer, 2015). Convection is driven by a thermal inversion at the base of the lithosphere, or thermal-rheological boundary layer (TBL) (e.g., Sleep, 2007). Thereby, the relevant local Rayleigh number Ra_{loc} of the base of the TBL systematically grows as the TBL grows with time, and convective instability occurs as soon as Ra_{loc} exceeds a critical Rayleigh number Ra_c (e.g., Turcotte & Schubert, 2002). Ra_c is ~1,000 for the preferred wave number w of convection (with $w = 2\pi h/\lambda$, where h is the thickness of the convective layer and λ the wavelength of a convection cell), but varies with w (Turcotte & Schubert, 2002). We compute the local Rayleigh number (Ra_{loc}) of the layer that potentially goes convectively unstable, i.e., the convective layer, and compare with the critical Rayleigh number (Ra_c):

$$Ra_{loc} = \frac{[\alpha(T_0 - T_{loc})\rho_0 - \Delta\rho_0]gh^3}{\kappa\eta_{loc}} \tag{14}$$

$$t_{onset} : Ra_{loc} > Ra_c \tag{15}$$

where α is the thermal expansivity, T_0 is the temperature at the LAB (e.g., 1300°C in most cases), T_{loc} is the temperature at the top of the TBL, ρ_0 is the reference density, $\Delta\rho_0$ is the compositional density difference between asthenospheric mantle and lithospheric mantle, g is the gravitational acceleration, h is the thickness of the convective layer (twice the thickness of the TBL; explained below), κ is the thermal diffusivity, η_{loc} is the relevant maximum viscosity at the top of the TBL, and t_{onset} is the onset time of convective instability. The thickness of the convective layer is the most important parameter which has the largest effect on the computed η_{loc}. We define the top of the TBL as the depth at which $\eta = \eta_{loc} = 2 \times 10^{21}$ Pa s, assuming that the stiff shallow part of the TBL does not contribute to convective instability. From a blank model (i.e., without producing convective instability, but otherwise analogous to the relevant model), we extract the averaged 1-D temperature and pressure profiles, based on which, we compute the depth at which $\eta = 2 \times 10^{21}$ Pa s using the flow laws of wet olivine (considering both dislocation and diffusion creep, equations (8)–(12) and Tables 1 and 2). We define the bottom of the TBL as the LAB (i.e., where the geotherm reaches the potential temperature of T_{LAB}). Thus, computing the thickness of the TBL, we explicitly take into account water content, mantle
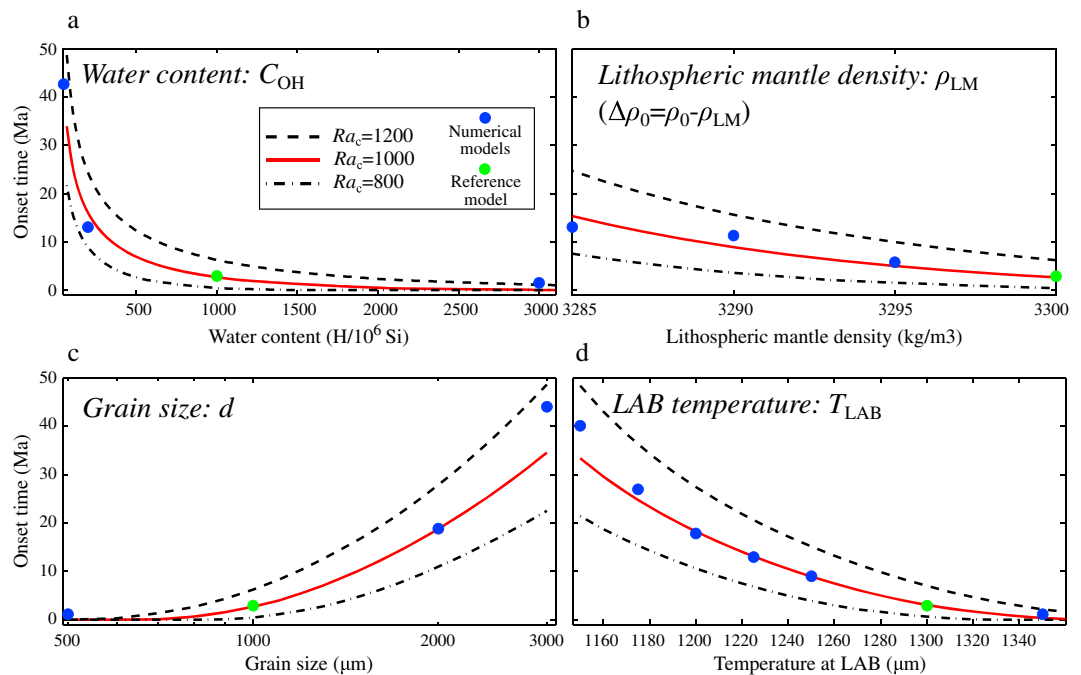
Figure 12. Semianalytical test of the onset time of convective instability using different model parameters. Numerical models are imposed in the plots. Effects of the four model parameters: (a) water content, (b) reference density of lithospheric mantle, (c) grain size, and (d) temperature at LAB. The onset time of convective instability of the numerical models is determined by the rapid increase of the averaged downwelling velocities.

potential temperature, the reference density of the lithospheric mantle, and grain size. The relevant thickness of the convective layer h is taken to be twice the thickness of the TBL, because the top of the asthenosphere also contributes to convection and assuming a ~1:1 aspect ratio of initial convection cells.

According to equations (14) and (15), we compute the onset time of convective instability as a function of parameters C_{OH}, ρ_{LM}, d, and T_{LAB}. Figure 12 shows a comparison of these semianalytical onset ages (lines) with those predicted by numerical experiments (filled circles). The three lines in each panel refer to slightly different Ra_c (i.e., 800, 1,000, and 1,200), and the predictions of almost all numerical models fall within these bounds as given by the semianalytic solutions. Ra_c is indeed expected to slightly vary from case to case, because Ra_c depends on w (see above) and only a given set of w are allowed in our restricted numerical-model domain. This interpretation of the observed variability in numerical model predictions is corroborated by a systematically reduced variability for the subset of cases with short onset ages. For short onset ages, h and λ tend to be small, and thus, convection cells can readily assume the most preferred w within a given width of the numerical domain. A test model without boundary extension (Figure 11) shows earlier lithospheric mantle dripping, which can be explained by the larger layer thickness (h) that gives larger thermal Rayleigh number.

4.2. Hydration-Driven Weakening of the Cratonic Lithosphere

Due to the high numerical resolution and short time steps used in this study, model running time is several tens of millions of years, which is much shorter than the relatively long destruction processes of some cratons. For example, the destruction of the North China craton lasted from the Jurassic to the Cretaceous (e.g., Menzies et al., 2007). Besides, when we start our numerical simulations, we assume that water has been transported into the cratonic lithosphere and distribute homogeneously. The prior deformation history and heterogeneous water distribution in the upper mantle are ignored. These model limitations are justified, since our study focuses on how water interplays with other parameters to facilitate cratonic thinning through convective instability.

Results of parameter tests indicate that lithospheric dripping is favored by high water content of olivine, dense lithospheric mantle, high temperature at the LAB, small grain size of olivine aggregates, and small values of mantle activation volume. The grain size of olivine varies between 0.1 mm and 10 mm in this study, which
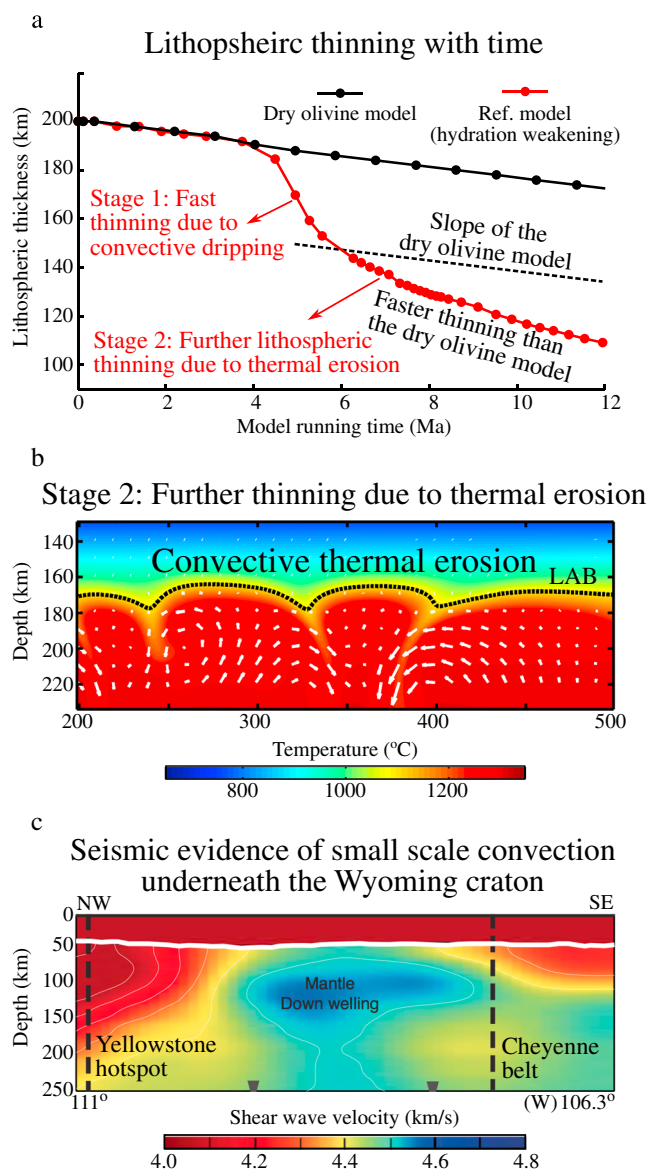
Figure 13. Cratonic lithospheric thinning and seismic evidence. (a) Two stages of lithospheric thinning. (b) Stage 2 of lithospheric thinning due to convective thermal erosion. (c) First seismic evidence of small-scale convection underneath the Wyoming craton (Dave & Li, 2016). See details of the profile in Dave and Li (2016).

falls in a reasonable range of peridotites (Karato, 2010). The relatively large density of lithospheric mantle and high temperature at the LAB will counteract if the major element composition of the lithospheric mantle is not significantly changed. Dry, depleted, and buoyant lithospheric mantle prevents cratonic roots from lithospheric dripping. However, for cratonic roots that have experienced intensive modification/fertilization in some regions (Folet, 2008; Koptev et al., 2015; Tappe et al., 2007), suitable conditions for lithospheric mantle dripping may form. For example, the depleted lithospheric mantle beneath the Eastern Block of the North China craton was subjected to significant metasomatism prior to lithospheric thinning (Zhang et al., 2009). The cratonic root beneath North America may have been dragged and detached from the craton center by mantle flow (Kaban et al., 2015). Density of the continental lithospheric mantle is generally less than the underlying asthenosphere because of depleted composition. However, Phanerozoic or metasomatized Fe-rich cratonic mantle may have higher density due to high content of garnet and reduced Fo number in olivine (Artemieva, 2009).

Cratonic lithospheric thinning due to hydration weakening can be summarized into two stages (Figure 13a). The first stage is fast lithospheric thinning due to the occurrence of convective instability, which has been largely discussed in the above sections. The second stage shows slower lithospheric thinning than that of the stage one, but lithospheric thinning is still faster than the model using dry olivine rheology (Figure 13a). This is caused by the continuous convective thermal erosion (Figure 13b). The occurrence of the convective thermal erosion after the vigorous lithospheric mantle dripping indicates that cratonic thinning is a long-term process, such as the North China craton (e.g., Menzies et al., 2007, Xu, 2007). Recently, the first seismic evidence of small-scale mantle convection beneath the Wyoming craton is revealed (Figure 13c) (Dave & Li, 2016). The formation of the small-scale mantle convection is likely promoted by slab dehydration of the flat Farallon subduction (e.g., Li et al., 2008). Thus, lithospheric mantle dripping (i.e., convective instability) driven by hydration weakening may play an important role in intraplate lithospheric thinning, such as the North China craton (Menzies et al., 1993, 2007), the Colorado Plateau (Li et al., 2008), and the Wyoming craton (Dave & Li, 2016).

5. Conclusions

We investigated the influence of hydration-induced weakening on the dynamics of cratonic lithosphere using wet olivine flow law for the mantle rheology and give the following conclusions.

1. Using only dislocation creep of wet olivine for mantle rheology, convective instability does not occur along the base of the cratonic lithosphere, although the lithospheric mantle has been largely weakened.
2. Employing both dislocation and diffusion creep of wet olivine for mantle rheology, convective instability occurs in the basal layer of the lithospheric mantle, and lithospheric mantle drips into the asthenospheric mantle resulting in a thinner cratonic lithosphere.
3. Model parameters influence the dynamics of convective instability. Semianalytical models are performed to predict the onset time of convective instability influenced by various parameters.
4. Dehydration of juxtaposed oceanic subduction slabs and long-term mantle metasomatism during craton evolution can cause hydration weakening of the cratonic lithosphere, promoting convective instability and lithospheric mantle dripping. Cratonic lithosphere can be thinned accordingly; faster lithospheric thinning during lithospheric mantle dripping followed by continuous and slower thinning due to thermal erosion.

References

Arcay, D., Tric, E., & Doin, M.-P. (2005). Numerical simulations of subduction zones: Effect of slab dehydration on the mantle wedge dynamics. *Physics of the Earth and Planetary Interiors*, *149*(1), 133–153. https://doi.org/10.1016/j.pepi.2004.08.020

Artemieva, I. M. (2009). The continental lithosphere: Reconciling thermal, seismic, and petrologic data. *Lithos*, *109*(1), 23–46.

Aubaud, C., Hauri, E. H., & Hirschmann, M. M. (2004). Hydrogen partition coefficients between nominally anhydrous minerals and basaltic melts. *Geophysical Research Letters*, *31*, L20611. https://doi.org/10.1029/2004GL021341

Bai, Q., Mackwell, S., & Kohlstedt, D. (1991). High-temperature creep of olivine single crystals 1. Mechanical results for buffered samples. *Journal of Geophysical Research*, *96*(B2), 2441–2463.

Bittner, D., & Schmeling, H. (1995). Numerical modeling of melting processes and induced diapirism in the lower crust. *Geophysical Journal International*, *123*, 59–70.

Borch, R., & Green, H. (1989). Deformation of peridotite at high pressure in a new molten salt cell: Comparison of traditional and homologous temperature treatments. *Physics of the Earth and Planetary Interiors*, *55*(3-4), 269–276.

Brune, S., Popov, A. A., & Sobolev, S. V. (2012). Modeling suggests that oblique extension facilitates rifting and continental break-up. *Journal of Geophysical Research*, *117*, B08402. https://doi.org/10.1029/2011JB008860

Buck, W. R. (2006). The role of magma in the development of the Afro-Arabian rift system. *Geological Society, London, Special Publications*, *259*, 43–54. https://doi.org/10.1144/GSL.SP.2006.259.01.05

Buck, W. R., Lavier, L. L., & Poliakov, A. N. B. (1999). How to make a rift wide? *Philosophical Transactions of the Royal Society of London, Series A*, *357*, 671–693. https://doi.org/10.1098/rsta.1999.0348

Burg, J.-P., & Gerya, T. (2005). The role of viscous heating in Barrovian metamorphism of collisional orogens: Thermomechanical models and application to the Lepontine dome in the Central Alps. *Journal of Metamorphic Geology*, *23*, 75–95. https://doi.org/10.1111/j.1525-1314.2005.00563.x

Burgmann, R., & Dresen, G. (2008). Rheology of the lower crust and upper mantle: Evidence from rock mechanics, geodesy, and field observations. *Annual Review of Earth and Planetary Sciences*, *36*, 531–567. https://doi.org/10.1146/annurev.earth.36.031207.124326

Carlson, R. W., Irving, A. J., Schulze, D. J., & Hearn Jr, B. C. (2004). Timing of Precambrian melt depletion and Phanerozoic refertilization events in the lithospheric mantle of the Wyoming Craton and adjacent Central Plains Orogen. *Lithos*, *77*, 453–472. https://doi.org/10.1016/j.lithos.2004.03.030

Carlson, R. W., Pearson, D. G., & James, D. E. (2005). Physical, chemical, and chronological characteristics of continental mantle. *Reviews of Geophysics*, *43*, RG1001. https://doi.org/10.1029/2004RG000156

Chen, H., Xia, Q.-K., Ingrin, J., Deloule, E., & Bi, Y. (2017). Heterogeneous source components of intraplate basalts from NE China induced by the ongoing Pacific slab subduction. *Earth and Planetary Science Letters*, *459*, 208–220. https://doi.org/10.1016/j.epsl.2016.11.030

Clauser, C., & Huenges, E. (1995). Thermal conductivity of rocks, minerals. In T. J. Ahrens (Ed.), *Rock Physics and Phase Relations* (pp. 105–126). Washington, DC: AGU.

Crameri, F. et al. (2012). A comparison of numerical surface topography calculations in geodynamic modelling: An evaluation of the 'sticky air' method. *Geophysical Journal International*, *189*, 38–54. https://doi.org/10.1111/j.1365-246X.2012.05388.x

Danderfer, A., De Waele, B., Pedreira, A. J., & Nalini, H. A. (2009). New geochronological constraints on the geological evolution of Espinhaço basin within the São Francisco Craton-Brazil. *Precambrian Research*, *170*(1), 116–128.

Dave, R., & Li, A. (2016). Destruction of the Wyoming craton: Seismic evidence and geodynamic processes. *Geology*, *44*, 883–886. https://doi.org/10.1130/G38147.1

Dixon, J. E., Dixon, T. H., Bell, D. R., & Malservisi, R. (2004). Lateral variation in upper mantle viscosity: Role of water. *Earth and Planetary Science Letters*, *222*, 451–467. https://doi.org/10.1016/j.epsl.2004.03.022

Djomani, Y. H. P., O'Reilly, S. Y., Griffin, W. L., & Morgan, P. (2001). The density structure of subcontinental lithosphere through time. *Earth and Planetary Science Letters*, *184*, 605–621.

Doucet, L. S., Peslier, A. H., Ionov, D. A., Brandon, A. D., Golovin, A. V., Goncharov, A. G., & Ashchepkov, I. V. (2014). High water contents in the Siberian cratonic mantle linked to metasomatism: An FTIR study of Udachnaya peridotite xenoliths. *Geochimica et Cosmochimica Acta*, *137*, 159–187.

Faccenda, M. (2014). Water in the slab: A trilogy. *Tectonophysics*, *614*, 1–30. https://doi.org/10.1016/j.tecto.2013.12.020

Faccenda, M., Gerya, T. V., Mancktelow, N. S., & Moresi, L. (2012). Fluid flow during slab unbending and dehydration: Implications for intermediate-depth seismicity, slab weakening and deep water recycling. *Geochemistry, Geophysics, Geosystems*, *13*, Q01010. https://doi.org/10.1029/2011GC003860

Foley, S. F. (2008). Rejuvenation and erosion of the cratonic lithosphere. *Nature Geoscience*, *1*, 503–510. https://doi.org/10.1038/ngeo261

Fullea, J., Muller, M. R., & Jones, A. G. (2011). Electrical conductivity of continental lithospheric mantle from integrated geophysical and petrological modeling: Application to the Kaapvaal Craton and Rehoboth Terrane, southern Africa. *Journal of Geophysical Research*, *116*, B10202. https://doi.org/10.1029/2011JB008544

Gao, S., Rudnick, R. L., Yuan, H., Liu, X., Liu, Y., Xu, W., ... Wang, Q. (2004). Recycling lower continental crust in the North China craton. *Nature*, *432*(7019), 892–897. https://doi.org/10.1038/nature03162

Gerya, T. V., & Yuen, D. A. (2003). Characteristics-based marker-in-cell method with conservative finite-differences schemes for modeling geological flows with strongly variable transport properties. *Physics of the Earth and Planetary Interiors*, *140*, 293–318. https://doi.org/10.1016/j.pepi.2003.09.006

Gorczyk, W., Hobbs, B., & Gerya, T. (2012). Initiation of Rayleigh-Taylor instabilities in intra-cratonic settings. *Tectonophysics*, *514-517*, 146–155. https://doi.org/10.1016/j.tecto.2011.10.016

Gueydan, F., & Précigout, J. (2014). Modes of continental rifting as a function of ductile strain localization in the lithospheric mantle. *Tectonophysics*, *612*, 18–25.

Hacker, B. R. (2008). H_2O subduction beyond arcs. *Geochemistry, Geophysics, Geosystems*, *9*, Q03001. https://doi.org/10.1029/2007GC001707

He, L. (2014). Numerical modeling of convective erosion and peridotite-melt interaction in big mantle wedge: Implications for the destruction of the North China Craton. *Journal of Geophysical Research*, *119*, 3662–3677. https://doi.org/10.1002/2013JB010657

Hirschmann, M. M. (2006). Water, melting, and the deep Earth H_2O cycle. *Annual Review of Earth and Planetary Sciences*, *34*, 629–653. https://doi.org/10.1146/annurev.earth.34.031405.125211

Hirth, G., & Kohlstedt, D. L. (2003). Rheology of the upper mantle and the mantle wedge: A view from the experimentalists. In Eiler, J. E. (Ed.), *Inside the Subduction Factory* (pp. 83–105). Washington, DC: AGU.

Huang, J., & Zhao, D. (2006). High-resolution mantle tomography of China and surrounding regions. *Journal of Geophysical Research*, *111*, B09305. https://doi.org/10.1029/2005JB004066

Kaban, M. K., Mooney, W. D., & Petrunin, A. G. (2015). Cratonic root beneath North America shifted by basal drag from the convecting mantle. *Nature Geoscience*, *8*, 797–801.

Karato, S. (1989). Grain growth kinetics in olivine aggregates. *Tectonophysics*, *168*(4), 255–273.

Karato, S. (1992). On the Lehmann discontinuity. *Geophysical Research Letters*, *19*(22), 2255–2258.

Karato, S. (2010). Rheology of the deep upper mantle and its implications for the preservation of the continental roots: A review. *Tectonophysics*, *481*, 82–98. https://doi.org/10.1016/j.tecto.2009.04.011

Karato, S., & Jung, H. (2003). Effects of pressure on high-temperature dislocation creep in olivine. *Philosophical Magazine*, *83*(3), 401–414. https://doi.org/10.1080/0141861021000025829

Karato, S., Rubie, D. C., & Yan, H. (1993). Dislocation recovery in olivine under deep upper mantle conditions' implications for creep and diffusion. *Journal of Geophysical Research*, *98*(B6), 9761–9768.

Kawazoe, T., Karato, S., Otsuka, K., Jing, Z., & Mookherjee, M. (2009). Shear deformation of dry polycrystalline olivine under deep upper mantle conditions using a rotational Drickamer apparatus (RDA). *Physics of the Earth and Planetary Interiors*, *174*, 128–137. https://doi.org/10.1016/j.pepi.2008.06.027

King, S. D., & Ritsema, J. (2000). African hot spot volcanism: Small-scale convection in the upper mantle beneath cratons. *Nature*, *290*, 1137–1140. https://doi.org/10.1126/science.290.5494.1137

Kohlstedt, D. L., Keppler, H., & Rubie, D. C. (1996). Solubility of water in the α, β and γ phases of $(Mg, Fe)_2SiO_4$. *Contributions to Mineralogy and Petrology*, *123*, 345–357.

Koptev, A., Calais, E., Burov, E., Leroy, S., & Gerya, T. (2015). Dual continental rift systems generated by plume–lithosphere interaction. *Nature Geoscience*, *8*, 388–392. https://doi.org/10.1038/NGEO2401

Lee, C.-T. (2005). Trace element evidence for hydrous metasomatism at the base of the North American lithosphere and possible association with Laramide low-angle subduction. *Journal of Geology*, *113*(6), 673–685.

Lee, C.-T. A., Luffi, P., & Chin, E. J. (2011). Building and destroying continental mantle. *Annu. Rev. Earth and Planetary Science*, *39*, 59–90. https://doi.org/10.1146/annurev-earth-040610-133505

Lenardic, A., Moresi, L.-N., & Muhlhaus, H. (2003). Longevity and stability of cratonic lithosphere: Insights from numerical simulations of coupled mantle convection and continental tectonics. *Journal of Geophysical Research*, *108*(B6), 2303. https://doi.org/10.1029/2002JB001859

Li, L., Weidner, D., Raterron, P., Jiuhua, C., Vaughan, M., Shenghua, M., & Durham, B. (2006). Deformation of olivine at mantle pressure using the D-DIA. *European Journal of Mineralogy*, *18*(1), 7–19.

Li, Z.-X. A., Lee, C.-T. A., Peslier, A. H., & Lenardic, A. (2008). Water contents in mantle xenoliths from the Colorado Plateau and vicinity: Implications for the mantle rheology and hydration-induced thinning of continental lithosphere. *Journal of Geophysical Research*, *113*, B09210. https://doi.org/10.1029/2007JB005540

Liao, J., & Gerya, T. (2014). Influence of lithospheric mantle stratification on craton extension: Insight from two-dimensional thermo-mechanical modeling. *Tectonophysics*, *631*, 50–64. https://doi.org/10.1016/j.tecto.2014.01.020

Liao, J., & Gerya, T. (2017). Partitioning of crustal shortening during continental collision: 2-D thermomechanical modeling. *Journal of Geophysical Research*, *122*, 592–606. https://doi.org/10.1002/2016JB013398

Liao, J., Gerya, T., & Wang, Q. (2013). Layered structure of the lithospheric mantle changes dynamics of craton extension. *Geophysical Research Letters*, *40*, 1–6. https://doi.org/10.1002/2013GL058081

Mackwell, S., Kohlstedt, D., & Paterson, M. (1985). The role of water in the deformation of olivine single crystals. *Journal of Geophysical Research*, *90*(B13), 11,319–11,333.

Manning, C. E. (2004). The chemistry of subduction-zone fluids. *Earth and Planetary Science Letters*, *223*(1), 1–16.

Mei, S., & Kohlstedt, D. (2000a). Influence of water on plastic deformation of olivine aggregates: 2. Dislocation creep regime. *Journal of Geophysical Research*, *105*(B9), 21,471–21,481.

Mei, S., & Kohlstedt, D. (2000b). Influence of water on plastic deformation of olivine aggregates: 1. Diffusion creep regime. *Journal of Geophysical Research*, *105*(B9), 21,457–21,469.

Menzies, M., Xu, Y. G., Zhang, H. F., & Fan, W. M. (2007). Integration of geology, geophysics and geochemistry: A key to understanding the North China Craton. *Lithos*, *96*, 1–21. https://doi.org/10.1016/j.lithos.2006.09.008

Menzies, M. A., Fan, W. M., & Zhang, M. (1993). Palaeozoic and Cenozoic lithoprobes and the loss of >120 kin of Archaean lithosphere, Sino-Korean craton, China. *Geological Society Special Publication*, *76*, 71–81.

Mitrovica, J., & Forte, A. (2004). A new inference of mantle viscosity based upon joint inversion of convection and glacial isostatic adjustment data. *Earth and Planetary Science Letters*, *225*(1), 177–189. https://doi.org/10.1016/j.epsl.2004.06.005

Motoki, M. H., & Ballmer, M. D. (2015). Intraplate volcanism due to convective instability of stagnant slabs in the mantle transition zone. *Geochemistry, Geophysics, Geosystems*, *16*, 538–551. https://doi.org/10.1002/2014GC005608

Ni, H., Zhang, L., Xiong, X., Mao, Z., & Wang, J. (2017). Supercritical fluids at subduction zones: Evidence, formation condition, and physicochemical properties. *Earth-Science Reviews*, *167*, 62–71.

Niu, Y. (2005). Generation and evolution of basaltic magmas: Some basic concepts and a new view on the origin of Mesozoic-Cenozoic basaltic volcanism in eastern China. *Geological Journal of China Universities*, *11*, 9–46.

O'Neill, C. J., Lenardic, A., & Griffin, W. L. (2008). Dynamics of cratons in an evolving mantle. *Lithos*, *102*, 12–24. https://doi.org/10.1016/j.lithos.2007.04.006

O'Neill, C. J., Kobussen, A., & Lenardic, A. (2010). The mechanics of continental lithosphere-asthenosphere coupling. *Lithos*, *120*, 55–62. https://doi.org/10.1016/j.lithos.2010.07.008

Peslier, A. H., Woodland, A. B., Bell, D. R., & Lazarov, M. (2010). Olivine water contents in the continental lithosphere and the longevity of cratons. *Nature*, *467*, 78–81. https://doi.org/10.1038/nature09317

Price, S., Russell, J., & Kopylova, M. (2000). Primitive magma from the Jericho Pipe, NWT, Canada: Constraints on primary kimberlite melt chemistry. *Journal of Petrology*, *41*(6), 789–808.

Ranalli, G. (1995). *Rheology of the Earth*. London, UK: Chapman & Hall.

Richard, G. C., & Bercovici, D. (2009). Water-induced convection in the Earth's mantle transition zone. *Journal of Geophysical Research*, *114*, B01205. https://doi.org/10.1029/2008JB005734

Rozel, A., Ricard, Y., & Bercovici, D. (2011). A thermodynamically self-consistent damage equation for grain size evolution during dynamic recrystallization. *Geophysical Journal International*, *184*(2), 719–728.

Selway, K., Yi, J., & Karato, S. (2014). Water content of the Tanzanian lithosphere from magnetotelluric data: Implications for cratonic growth and stability. *Earth and Planetary Science Letters*, *388*, 175–186. https://doi.org/10.1016/j.epsl.2013.11.024

Sleep, N. H. (2005). Evolution of the continental lithosphere. *Annu. Rev. Earth Planet. Sci.*, *33*, 369–393. https://doi.org/10.1146/annurev.earth.33.092203.122643

Sleep, N. H. (2007). Evolution of the Earth: Plate tectonics through time. In N. H. Sleep (Eds.), *Treatise on Geophysics* (Vol. 9, pp. 145–169). Amsterdam: Elsevier.

Sleep, N. H. (2009). Stagnant lid convection and carbonate metasomatism of the deep continental lithosphere. *Geochemistry, Geophysics, Geosystems*, *10*, Q11010. https://doi.org/10.1029/2009GC002702

Smith, D. (2010). Antigorite peridotite, metaserpentinite, and other inclusions within diatremes on the Colorado Plateau, SW USA: Implications for the mantle wedge during low-angle subduction. *Journal of Petrology*, *51*(6), 1355–1379. https://doi.org/10.1093/petrology/egq022

Steinberger, B., & Calderwood, A. R. (2006). Models of large-scale viscous flow in the Earth's mantle with constraints from mineral physics and surface observations. *Geophysical Journal International*, *167*, 1461–1481.

Tappe, S., Foley, S. F., Stracke, A., & Romer, R. L. (2007). Craton reactivation on the Labrador Sea margins: $^{40}Ar/^{39}Ar$ age and Sr-Nd-Hf-Pb isotope constraints from alkaline and carbonatite intrusives. *Earth and Planetary Science Letters*, *256*, 433–454. https://doi.org/10.1016/j.epsl.2007.01.036

Tielke, J. A., Zimmerman, M. E., & Kohlstedt, D. L. (2017). Hydrolytic weakening in olivine single crystals. *Journal of Geophysical Research*, *122*, 3465–3479. https://doi.org/10.1002/2017JB014004

Turcotte, D. L., & Schubert, G. (2002). *Geodynamics*. Cambridge, UK: Cambridge Univ. Press.

van Wijk, J. W., Baldridge, W. S., van Hunen, J., Goes, S., Aster, S., Coblentz, D. D., . . . Ni, J. (2010). Small-scale convection at the edge of the Colorado Plateau: Implications for topography, magmatism, and evolution of Proterozoic lithosphere. *Geology*, *38*, 611–614. https://doi.org/10.1130/G31031.1

Wang, Q. (2010). A review of water contents and ductile deformation mechanisms of olivine: Implications for the lithosphere-asthenosphere boundary of continents. *Lithos*, *120*, 30–41. https://doi.org/10.1016/j.lithos.2010.05.010

Wang, Q., Bagdassarov, N., Xia, Q., & Zhu, B. (2014). Water contents and electrical conductivity of peridotite xenoliths from the North China Craton: Implications for water distribution in the upper mantle. *Lithos*, *189*, 105–126. https://doi.org/10.1016/j.lithos.2013.08.005

Wang, Z., Kusky, T. M., & Capitanio, F. A. (2016). Lithosphere thinning induced by slab penetration into a hydrous mantle transition zone. *Geophysical Research Letters*, *43*, 11,567–11,577. https://doi.org/10.1002/2016GL071186

Weeraratne, D. S., Forsyth, D. W., Fischer, K. M., & Nyblade, A. A. (2003). Evidence for an upper mantle plume beneath the Tanzanian craton from Rayleigh wave tomography. *Journal of Geophysical Research*, *108*(B9), 2427. https://doi.org/10.1029/2002JB002273

Wu, F.-Y., Lin, J.-Q., Wilde, S. A., Zhang, X., & Yang, J.-H. (2005). Nature and significance of the Early Cretaceous giant igneous event in eastern China. *Earth and Planetary Science Letters*, *233*(1), 103–119. https://doi.org/10.1016/j.epsl.2005.02.019

Xia, Q. K., Liu, J., Liu, S. C., Kovacs, I., Feng, M., & Dang, L. (2013). High water content in Mesozoic primitive basalts of the North China Craton and implications on the destruction of cratonic mantle lithosphere. *Earth and Planetary Science Letters*, *361*, 85–97. https://doi.org/10.1016/j.epsl.2012.11.024

Xu, Y. G. (2001). Thermo-tectonic destruction of the Archaean lithospheric keel beneath the Sino-Korean Craton in China: Evidence, timing and mechanism. *Physics and Chemistry of the Earth (A)*, *26*(9-10), 747–757.

Xu, Y. G. (2007). Diachronous lithospheric thinning of the North China Craton and formation of the Daxin'anling–Taihangshan gravity lineament. *Lithos*, *96*(1), 281–298. https://doi.org/10.1016/j.lithos.2006.09.013

Xu, Y. G., Li, H., Pang, C., & He, B. (2009). On the timing and duration of the destruction of the North China Craton. *Chinese Science Bulletin*, *54*, 3379–3396. https://doi.org/10.1007/s11434-009-0346-5

Zhang, H. F., Sun, M., Zhou, X. H., & Ying, J. F. (2005). Geochemical constraints on the origin of Mesozoic alkaline intrusive complexes from the North China Craton and tectonic implications. *Lithos*, *1*, 297–317. https://doi.org/10.1016/j.lithos.2004.12.015

Zhang, H., Goldstein, S. L., Zhou, X., Sun, M., & Cai, Y. (2009). Comprehensive refertilization of lithospheric mantle beneath the North China Craton: further Os–Sr–Nd isotopic constraints. *Journal of the Geological Society of London*, *166*(2), 249–259. https://doi.org/10.1144/0016-76492007-152

Zheng, Y., Chen, R., Xu, Z., & Zhang, S. (2016). The transport of water in subduction zones. *Science China Earth Sciences*, *59*(4), 651–682.